Chemical Engineering Journal 487 (2024) 150465

Contents lists available at ScienceDirect

Chemical Engineering Journal

journal homepage: www.elsevier.com/locate/cej

Hierarchical porous nanofibers comprising N-doped graphitic C and ZIF-8 derived hollow N-doped C nanocages for long-life K-ion battery anodes

Jae Seob Lee [a,b], Narasimharao Kitchamsetti [a], Jung Sang Cho [a,*]

[a] Department of Engineering Chemistry, Chungbuk National University, Chungbuk 361-763, Republic of Korea
[b] Department of Materials Science and Engineering, Korea University, Anam-Dong, Seongbuk-Gu, Seoul 136-713, Republic of Korea

ARTICLE INFO

Keywords:
Electrospinning
Zeolitic imidazolate framework-8
Hollow nitrogen-doped carbon nanocage
Graphitic carbon
Potassium-ion batteries

ABSTRACT

Hierarchical porous carbon nanofibers (NFs) are designed *via* electrospinning, followed by simple carbonization, and applied as the anode for K-ion batteries (KIBs). The carbonization process is optimized to simultaneously satisfy sufficient graphitization of polyacrylonitrile (PAN)-derived soft carbon and complete conversion of zeolitic imidazolate framework-8 (ZIF-8) to hollow N-doped C nanocages. The prepared NFs through an optimized carbonization consists of porous and hollow N-doped C nanocages, which are encapsulated within the conductive graphitic carbon (GC) matrix, that acts as an efficient electron transport pathway. Moreover, the interconnected porous and hollow nanocages ensure a high contact area between the electrode and electrolyte and reduces the K-ion diffusion length. The N-doped GC with high electrical conductivity in the structure demonstrates reinforcing structural integrity as well as providing additional transport pathways for the unique electron transport. Therefore, the hierarchical porous carbon NFs show outstanding energy storage properties, such as stable cycle performance up to 10,000 cycles at the high current density of 1.0 A g^{-1} with high areal loading mass (1.8–1.9 mg cm^{-2}) of the active material, which clearly suggests the structural advantages of the nanostructure introduced in this study.

1. Introduction

Lithium-ion batteries (LIBs) have demonstrated great achievements as rechargeable batteries in recent years [1–3]. However, the inherent limitations of lithium, including uneven distribution, escalating prices, and constrained lithium storage capacity, necessitate exploration into alternative battery technologies with superior attributes. These attributes encompass prolonged cycling lifespan, heightened energy density, and cost-effectiveness [4–7]. One promising contender for replacing LIBs is the K-ion batteries (KIBs), which has garnered considerable research interest. KIBs have advantageous features including a relatively low redox potential (–2.93 V vs. E°) similar to lithium (–3.04 V vs. E°) and the abundance of potassium reserves, facilitating cost-effective manufacturing [8,9]. However, the larger ionic radius of K-ions (1.38 Å vs. 0.76 Å for Li-ion) presents challenges in terms of reversible potassiation/depotassiation of the active electrode and sluggish kinetics during discharge/charge processes. Nonetheless, KIBs remain a compelling subject of study for achieving economical and high-performance energy storage solutions [8,9].

Carbonaceous materials, including graphite, amorphous carbon, carbon nanotubes (CNTs), and graphene have emerged as promising anode materials for K-ion storage, paralleling their utilization in LIBs [5,10]. These materials hold appeal due to their affordability, chemical stability, and thermal resistance, positioning them as potential commercial anode candidates for KIBs [11,12]. However, carbon-based anode materials for KIBs encounter challenges compared to LIBs, attributed to increased steric resistance, restricted ionic diffusivity, and diminished energy density resulting from the larger ionic radius of K-ions in relation to interlayer spacing and atomic weight. To enhance the energy storage capabilities of carbonaceous materials in KIBs, ongoing research endeavors center around incorporating porous, hollow structures, and various nanoscale design strategies [13,14]. The integration of a porous network, particularly one facilitating electrolyte permeation into the carbonaceous structure, assumes a pivotal role in minimizing the diffusion path of K-ions within the layered configuration. This consequently enables rapid potassium insertion, resulting in augmented reversible capacity and rate performance [13,14].

In recent decades, metal–organic frameworks (MOFs)-derived porous carbons have been extensively explored for energy storage and conversion applications [15,16]. These materials, with their porous

* Corresponding author.
E-mail address: jscho@cbnu.ac.kr (J.S. Cho).

https://doi.org/10.1016/j.cej.2024.150465

Available online 15 March 2024

nature, high surface area, distinctive architectures, and tunable metallic compounds, hold promise. Furthermore, the controlled decomposition of MOFs under optimized conditions can yield graphite-like carbon products with heteroatom doping and open diffusion channels. Heteroatom doping, such as O, S, N, and P, can modulate the electronic structure of carbon materials, inducing defects in the graphitic carbon (GC) layer and enhancing reversible capacity [17–19]. Yang et al. studied Al-based MOF derived O/N-doped porous hard carbon materials with improved interlayer spacing (i.e., 0.39 nm) [19]. The graphitization degree of carbon is expected to increase with increase in temperature, thereby affecting the intercalation reaction and resulting in remarkable electrochemical performance [14]. Rui et al. prepared ultrathin MoS_2 nanosheets decorated cobalt nanoparticles confined porous carbon polyhedral with dense nitrogen doped CNTs backbone. The ZIF-67-C@MoS_2 composite exhibits a high reversible capacity of 199.8 mA h g^{-1} after 50 cycles at a current density of 100 mA g^{-1} with the Coulombic efficiency of close to 100 % [20].

In this study, we present a novel approach to achieve hierarchical porous nitrogen-doped carbon nanofibers (P-N-C NFs) by combining polyacrylonitrile (PAN)-derived nitrogen-doped GC (NGC) and ZIF-8-derived hollow nitrogen-doped carbon (N-C) nanocages. This composite serves as an ultra-long-life anode for KIBs. The NGC matrix, rich in ion-permeable defects, is achieved through a meticulously designed carbonization process of PAN, ensuring a well-developed graphitic structure. Simultaneously, ultrafine ZIF-8 polyhedra within PAN fibers act as sacrificial templates, forming interconnected porous and hollow N-C nanocages that facilitate electrolyte penetration. The nitrogen dopant in the GC matrix and hollow nanocages ensures enhanced electrical conductivity and rapid ionic/electronic transfer, thus promoting redox processes. We conduct a comprehensive analysis of the morphologies, characteristics, and electrochemical performance of P-N-C NFs comprising NGC and hollow nanocages, formed at various carbonization temperatures (800, 1000, and 1200 ℃), in comparison with non-porous carbon nanofibers. This study sheds light on the potential of these hierarchical porous nitrogen-doped carbon nanofibers as advanced anode materials for KIBs, providing valuable insights into their unique nanostructures and electrochemical behaviors.

2. Experimental section

2.1. Sample preparation

Hierarchical P-N-C NFs comprising PAN derived NGC and ZIF-8 derived hollow N-C nanocages were prepared by simple electrospinning followed by carbonization. Firstly, ZIF-8 polyhedra were produced by a solution route as reported earlier [21]. Briefly, 1.6 g of 2-methylimidazole (Thermo Fisher Scientific, 99 %) was added in 40 mL of methanol (SAMCHUN, 99.8 %) to form solution A under constant stirring. Further, 0.732 g of $Zn(NO_3)_2{\cdot}6H_2O$ (SAMCHUN, 98 %) was dissolved in 30 mL of methanol under constant stirring to form solution B. Thereafter solution A was added drop by drop to the solution B, which was blended for 6 h. Lastly, the resultant solution was washed three times through ethanol and centrifugation and dried overnight at 60 ℃ to obtain the desired ZIF-8 polyhedra. Moreover, to prepare the electrospinning solution, 2.0 g of obtained ZIF-8 polyhedra was dispersed in 20 mL of N,N-Dimethylformamide (DMF, SAMCHUN, 99.5 %) with the help of ultrasonication and stirred for some time. Subsequently, 2.0 g of PAN (Sigma-Aldrich, M_w = 150,000) was added slowly to the DMF/ZIF-8 solution and allowed to blend overnight at room temperature to achieve a uniform solution. The electrospinning solution was filled in a 12 mL plastic syringe equipped with a 21-gauge stainless steel needle. The spinning solution was ejected at a rate of 4 mL h^{-1} onto a drum collector covered by Al foil rotating at the speed of 180 rpm. The distance and applied voltage between the collector and tip of the needle were 18 cm and 24 kV, respectively. The resulting ZIF-8/PAN composite NFs were kept for stabilization at 150 ℃ for 2 days in a hot air oven. Furthermore, the stabilized NFs were carbonized once at different temperatures ranging from 800, 1000, and 1200 ℃ for 5 h in N_2 atmosphere to get desired P-N-C NFs, abbreviated as P-N-C-800, P-N-C-1000, and P-N-C-1200, respectively. For comparison, a non-porous N-C NFs (abbreviated as PAN-C) were also prepared using electrospinning in the absence of ZIF-8 polyhedra. As-spun PAN NFs were stabilized using two-step process to prevent agglomeration of the NFs. The first step was performed at 150 ℃ for 2 days, followed by second step at 250 ℃ for 1 h under air atmosphere. After the stabilization, the carbonization was carried out at 1000 ℃ in a N_2 atmosphere for 5 h.

3. Results and discussion

The hierarchical porous nanofibers, constructed using PAN-derived NGC matrix and ZIF-8-derived hollow N-C nanocages, were prepared employing an electrospinning technique followed by a one-step carbonization process. The detailed synthetic mechanism of the unique nanostructure is systematically described in Scheme 1. A spinning solution based on DMF containing PAN and ZIF-8 polyhedra was electrospun, leading to the uniform dispersion of ZIF-8 polyhedra (ϕ = 60 nm) within the PAN matrix, forming ZIF-8/PAN composite NFs (Scheme 1a-①). The resulting ZIF-8/PAN composite NFs were thermally stabilized at 150 ℃ and then subjected to one-step carbonization at different temperatures (800, 1000, 1200 ℃) for 5 h in a N_2 atmosphere, respectively. During the carbonization process, the ZIF-8 polyhedra consisting of central Zn atom and the N-rich organic ligand (e.g., 2-methylimidazole) are decomposed into highly volatile Zn/Zn^{2+} metal and interconnected with hollow N-C nanocages. Simultaneously, the heat-induced decomposition of the PAN into the NGC framework led to the contraction of the nanofiber structure, tightly packing the hollow nanocages and forming chain-like nanofibers. Notably, the carbonization temperature significantly influenced the critical factors for optimal porous composite NFs as anode materials for KIBs: the nitrogen content in hollow N-C nanocages, the volatilization of Zn metal species, and the adequate graphitization of the PAN-derived soft carbon matrix. The composite NFs obtained at 800 ℃ (P-N-C-800; Scheme 1a-②) exhibit traces of metallic-Zn species within the hollow N-C nanocages due to the insufficient temperature, resulting in an NGC-deficient carbon matrix. The composite NFs carbonized at 1000 ℃ (P-N-C-1000; Scheme 1a-③) contain hollow N-C nanocages with complete sublimation of metallic-Zn species due to the optimal temperature and PAN-derived NGC matrix. Furthermore, by increasing the carbonization temperature to 1200 ℃, the N-dopants derived from the imidazole units in the hollow N-C nanocages are removed due to high temperature, generating composite NFs comprising hollow C nanocages and an NGC-rich matrix (P-N-C-1200; Scheme 1a-④). The detailed mechanism for the change of N content and volatilization of Zn metal species via the evolution of structural changes in ZIF-8 polyhedra into hollow C nanocages concerning temperature is presented in Scheme 1b. Briefly, as the reaction temperature increases from room temperature to 300 ℃, N-rich organic linkers in ZIF-8 polyhedra carbonized into a stable N-doped C moieties as a carbon layer over the surface. With a further increase in temperature to 600 ℃, the Zn atoms in the ZIF-8 polyhedra are converted to highly volatile Zn/Zn^{2+} metals and rigid carbon layer resulting from overall organic linkers drags polyhedral surface outward. When the temperature reaches 800 ℃, the outward shrinkage process intensifies due to the continuous volatilization of metallic-Zn, leading to the collapse of the entire inner core of ZIF-8 and the gradual formation of hollow N-C nanocages. At 1000 ℃, metallic Zn is completely evaporated, resulting in hollow N-C nanocages with dense carbon shell. Further increasing the temperature to 1200 ℃ led to the removal of N-dopants, leaving only hollow C nanocages. Hence, it is believed that the porous composite NFs comprising the optimized carbonized hollow N-C nanocages and NGC matrix are capable of functioning as a network of interconnected conductive pathways. This network facilitates swift K-ion migration, enables efficient electrolyte infiltration, and ensures structural stability.

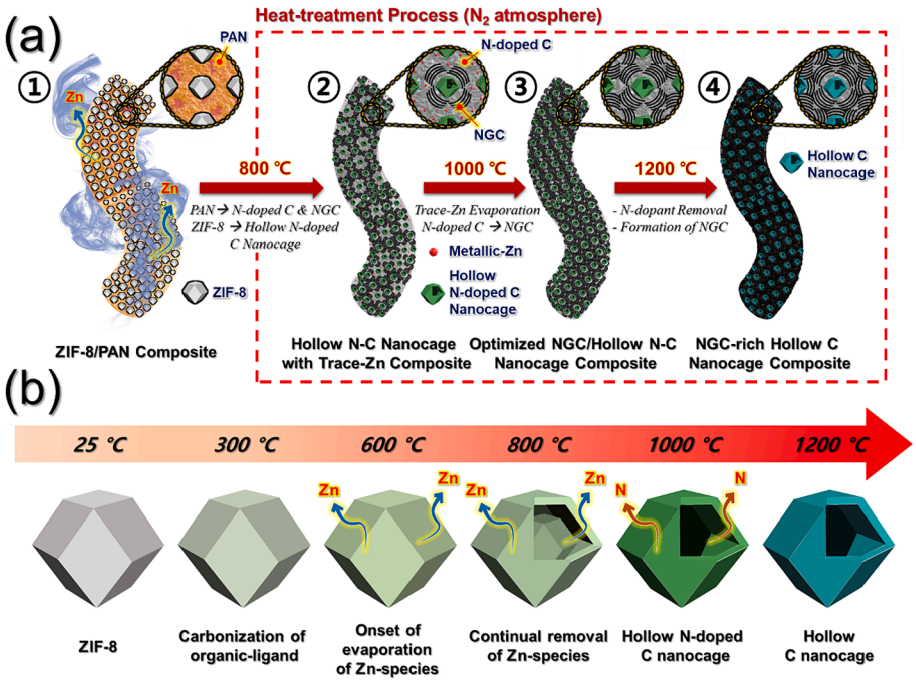

Scheme 1. (a) Formation mechanism of porous N-doped C NFs comprising NGC and hollow N-C nanocages and (b) detailed mechanism involving the structural evolution of ZIF-8 polyhedra to the hollow N-C nanocages as a function of temperature.

As a result, these composite NFs have the potential to significantly enhance the overall performance of K-ion storage.

To further understand the formation mechanism, comprehensive morphology and crystal structure analyses were performed on the products obtained after each process. The physical characterization results (including XRD, TGA, and FE-SEM analysis) of the ZIF-8 polyhedra prepared for the synthesis of PAN/ZIF-8 composite NFs are shown in Fig. S1. The FE-SEM image (Fig. S1a) of the ZIF-8 polyhedra prepared using co-precipitation of $Zn(NO_3)_2{\cdot}6H_2O$ and 2-methylimidazole in the presence of methanol shows a well-dispersed polyhedral morphology of ZIF-8 with a size distributions varying from 50 to 60 nm. Furthermore, the XRD pattern displayed in Fig. S1b reveals the strong and well-resolved peaks of the as-prepared ZIF-8 polyhedra, which are in line with the available reports on ZIF-8 polyhedra [22,23]. The presence of highly intense peaks located at (011), (002), (112), (022), (013), (222), (233), and (134) confirms the successful formation of ZIF-8 polyhedra. In addition, to confirm the detailed thermal decomposition mechanism of ZIF-8 polyhedra, TGA was conducted on the ZIF-8 polyhedra in an inert atmosphere as shown in Fig. S1c. The initial weight loss below 300 ℃ is attributed to the partial carbonization of organic ligand in the ZIF-8 structure. The gradual weight loss between 300 and 600 ℃ suggests the continuous carbonization of overall ZIF-8 polyhedra as the temperature increases. Subsequent weight loss beyond 600 ℃ is attributed to the volatilization of metallic-Zn from the ZIF-8 structure. The additional decomposition observed at higher temperatures corresponds to the release of N-containing gases. The thermal characteristics of the ZIF-8 polyhedra, as determined by thermogravimetric analysis, can provide insights into determining the heat-treatment temperature of subsequent PAN/ZIF-8 composite nanofibers.

Structural and morphological analyses were performed to further investigate the formation of the composite NFs comprising ZIF-8 polyheda within the PAN matrix after electrospinning. The XRD, FE-SEM and TG-mass spectrometry (TG-MS) results of the spun ZIF-8/PAN composite NFs obtained after stabilization at 150 ℃ are illustrated in Fig. 1. The FE-SEM image shown in Fig. 1a reveals the continuous 1D fibrous morphology formation with an average diameter of 600 nm. Moreover, the rough surface of the NFs indicates a uniform distribution of the ZIF-8

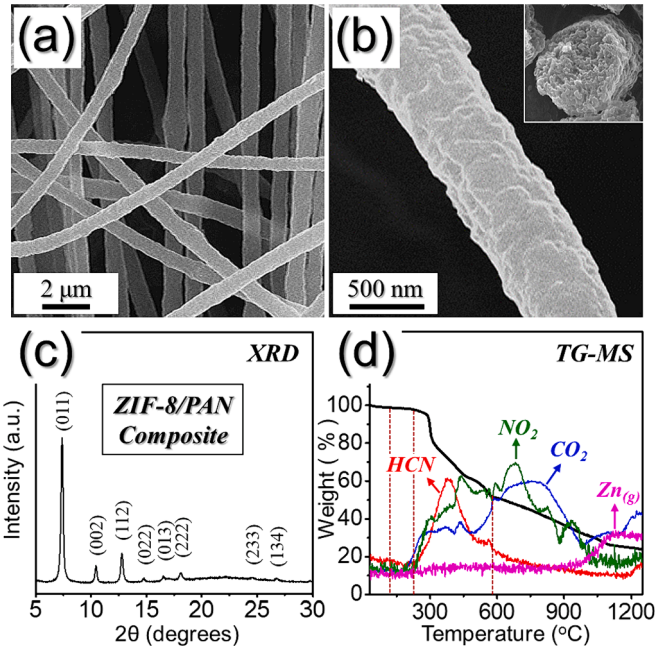

Fig. 1. (a,b) FE-SEM images, (c) XRD pattern, and (d) TG-MS curve (N_2 atmosphere) of the as-spun ZIF-8/PAN composite nanofibers obtained after stabilization at 150 ℃.

polyhedra in the PAN matrix (Fig. 1b). The cross-sectional diagram displayed in the inset of Fig. 1b also validates the uniform distribution of the ZIF-8 polyhedra inside the NFs suggesting the presence of highly ordered filled structure throughout the surface of NFs. In addition, the XRD patterns of the ZIF-8/PAN composite NFs illustrated in Fig. 1c reveal strong and well-resolved peaks that can be subjected to the ZIF-8 polyhedra, consistent with the XRD analysis of the as-prepared ZIF-8 polyhedra (Fig. S1b). The high-intensity peaks observed in the XRD patterns provide information about the existence of ZIF-8 polyhedra

within the fibrous structure. To establish reasonable temperature conditions of carbonization process for the synthesis of P-N-C NFs, TG-MS was performed under N_2 atmosphere (Fig. 1d). The TG-MS curves reveals the weight loss with respect to various temperature regions. The removal of moisture and crystal water in the NFs is occurred in the low-temperature region (i.e., ≤110 ℃). Similarly, HCN gas release by the carbonization activity of the PAN (220–580 ℃) and NO_2/CO_2 gases from the pyrolysis of the organic ligands (i.e., 2-methylimidazole units) of the ZIF-8 polyhedra (220–850 ℃) is continued parallelly in the mid-temperature range. In the high-temperature range (800–1200 ℃), the highly volatile reduced Zn/Zn^{2+} species within the ZIF-8 polyhedra are evaporated to form interconnected hollow N-C nanocages throughout the NF structure. Additionally, weight loss was observed in the region above 1000 ℃ due to the removal of the N-dopant in the hollow N-C nanocages by continuous NO_2 gas release. The TG-MS plot indicates that the stabilized ZIF-8/PAN composite NFs convert into highly porous carbon fibers containing interconnected chain-like hollow N-C nanocages with open pores at temperatures around 1000 ℃. Based on the TG-MS results, the carbonization of the stabilized ZIF-8/PAN composite NFs were carried out at various temperatures ranging from 800, 1000, and 1200 ℃ for 5 h in N_2 atmosphere to compare obtained P-N-C NFs.

To compare P-N-C NFs obtained at various temperature of carbonization, firstly, morphology and microstructural analysis of P-N-C NFs derived at 800 ℃ (P-N-C-800 NFs) were performed shown in Fig. 2. The FE-SEM image in Fig. 2a reveals the shrinkage of 1D fibrous structure of P-N-C-800 NFs after carbonization due to the thermal decomposition of PAN and the NFs had an average diameter of 450 nm. The cross-sectional FE-SEM (inset of Fig. 2a) and the bright regions in the TEM image (Fig. 2b) clearly suggest the presence of highly ordered pores throughout the surface of NFs. The pores originate from interconnected hollow N-C nanocages due to the removal of volatile reduced Zn and subsequent outward contraction during carbonization, suggesting that numerous hollow N-C nanocages are homogeneously distributed inside the carbon network. TEM analysis (Fig. 2c) obviously indicates the existence of evenly distributed hollow N-C nanocages with an average diameter of 30 nm. The high-resolution TEM (HR-TEM) image illustrated in Fig. 2d clearly suggests the lattice fringe spacing of metallic-Zn and NGC separated by 0.25 nm and 0.34 nm for the (002) and (002) crystal planes, respectively. In general, it is suggested that the formation of hollow N-C nanocages under sufficient temperature conditions is due to the acceleration effect of volatilization of internal metallic-Zn through pores formed by evaporation of metallic-Zn on the surface of ZIF-8, as reported in previous reports [24]. However, an insufficient temperature condition of 800 ℃ resulted in the formation of hollow N-C nanocages containing negligible amounts of quantum dot-sized metallic-Zn (<3nm). The presence of trace amounts of NGC observed in HR-TEM was produced by weak graphitization of soft carbon species derived from PAN, which will be explained later. The selected area electron diffraction (SAED) pattern confirms the presence of carbonaceous materials derived from PAN shown in Fig. 2e, and two defined diffraction rings can be allocated to the (002) and (101) planes of NGC in the NFs. In addition, the XRD pattern shown in Fig. 2f confirms two broad peaks

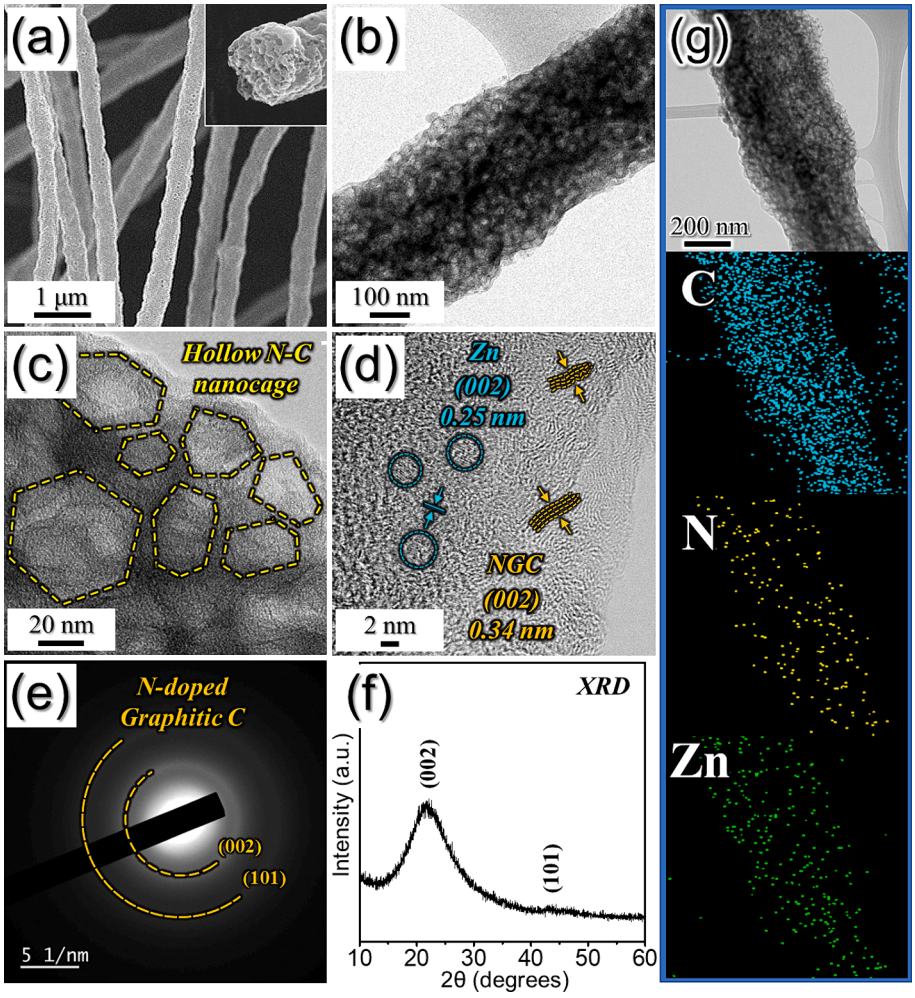

Fig. 2. Morphologies, SAED, XRD patterns, and elemental mapping images of the P-N-C-800 NFs obtained after heat-treatment at 800 ℃ under N_2 atmosphere of as-spun fibers: (a) FE-SEM images, (b,c) TEM images, (d) HR-TEM image, (e) SAED pattern, (f) XRD pattern, and (g) elemental mapping images.

observed at 23° and 42°, which are assigned to the (002) and (101) reflections of NGC originating from PAN, indicating that P-N-C-800 NFs were mostly constructed of carbonaceous materials. Therefore, the existence of trace amounts of metallic-Zn in the NFs was further verified through elemental mapping images shown in Fig. 2g. Moreover, the component of N observed in the carbon matrix of the 1D fibrous structure was initiated from the decomposition of PAN and organic ligands species in ZIF-8, and the N content quantified from the EA results (Table S1) was 12.1 wt%.

To establish the change in the characteristic of P-N-C NFs under higher temperature than 800 ℃, P-N-C-1000 NFs were obtained by the same carbonization condition except for the temperature of 1000 ℃, and the morphology and microstructure of P-N-C-1000 NFs were investigated shown in Fig. 3. The FE-SEM image shown in Fig. 3a reveals that fibrous structures with an average diameter of 430 nm are uniformly formed after carbonization process. It is noteworthy that the slightly shrunken fiber diameter of the P-N-C-1000 NFs compared to that of P-N-C-800 NFs (ϕ = 450 nm; Fig. 2a) is attributed to the higher temperature conditions. Additionally, the cross-sectional FE-SEM (inset of Fig. 3a) and TEM (Fig. 3b) images indicate the existence of interconnected pores throughout the fibrous structure. The mesoporous nature of NFs was attributed to the continuous transformation of ZIF-8 polyhedrons into hollow N-C nanocages. The TEM image shown in Fig. 3c clearly displays polygonal hollow N-C nanocages with an average diameter of 30 nm uniformly distributed in the NFs, supporting above statement. The HR-TEM image (Fig. 3d) shows the lattice fringe spacing of 0.34 nm corresponding to the (002) crystal plane of NGC matrix attributed to the PAN. In addition, it demonstrates complete evaporation of metallic-Zn species from the hollow N-C nanocages by sufficient temperature conditions. The SAED pattern displayed in Fig. 3e reveals distinct diffraction rings corresponding to the (002) and (101) planes associated with NGC, which are in great agreement with the XRD results. The XRD pattern (Fig. 3f) shows two diffraction peaks assigned to the carbonaceous material without any other impurity peaks, confirming the formation of hierarchical P-N-C-1000 NFs. Moreover, the elemental mapping image shown in Fig. 3g suggests that the P-N-C-1000 NFs is a porous 1D fiber consisting of only N and C without any Zn impurity. The N content from P-N-C-1000 NFs containing NGC matrix and hollow N-C nanocages was 4.7 wt%, which was quantified by EA analysis (Table S1). The hollow N-C nanocage without any Zn impurities effectively facilitates the permeation of electrolyte in P-N-C-1000 NFs reducing the diffusion pathway of K-ions, and promotes rapid redox reaction with improved electrical conductivity by N dopant. Therefore, it is believed that P-N-C-1000 NFs containing an NGC matrix imparting structural integrity and hollow N-C nanocage can exhibit to show improved performance as anode materials for KIBs.

To investigate in detail the effect of a higher carbonization temperature condition for 1200 ℃ on P-N-C NFs, P-N-C-1200 NFs were also prepared by carbonization at 1200 ℃ for 5 h in a N_2 environment, as shown in Fig. S2. The low-magnification FE-SEM image of P-N-C-1200 NFs shown in Fig. S2a displays a uniform 1D fibrous structure, similar to the FE-SEM images of P-N-C-800 and P-N-C-1000 NFs (Fig. 2a and 3a).

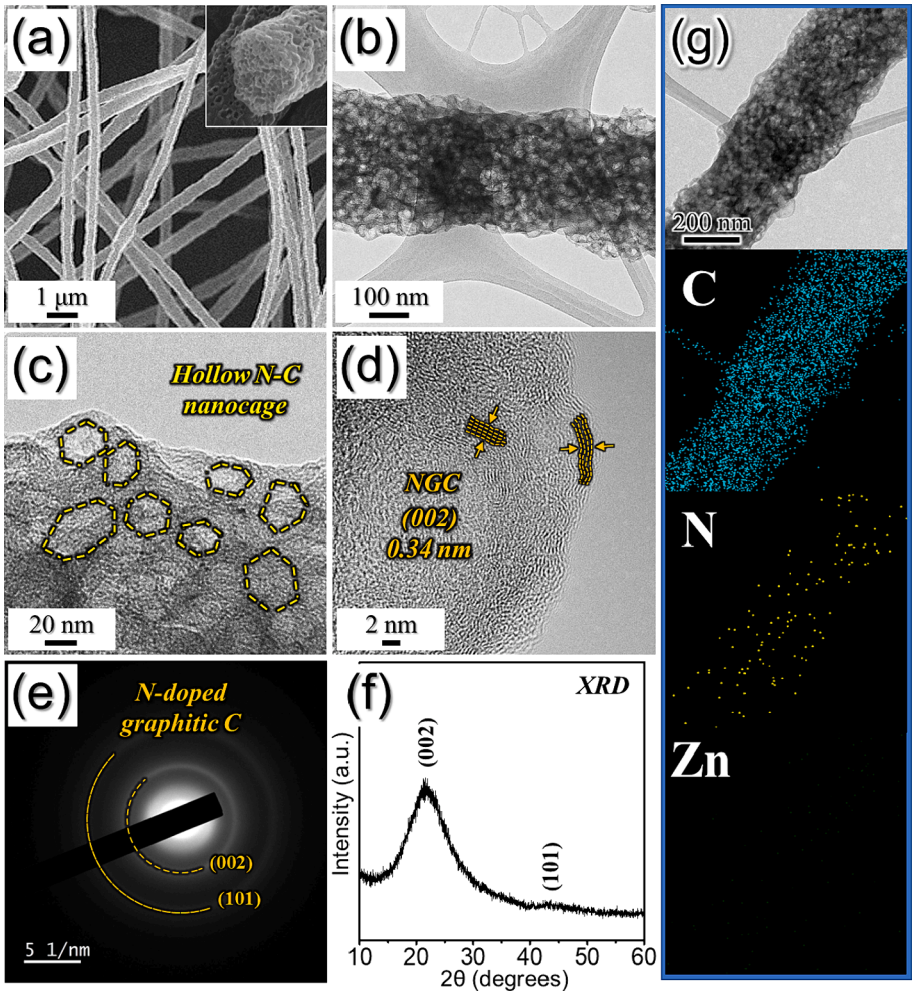

Fig. 3. Morphologies, SAED, XRD patterns, and elemental mapping images of the P-N-C-1000 NFs obtained after heat-treatment at 1000 ℃ under N_2 atmosphere of as-spun fibers: (a) FE-SEM images, (b,c) TEM images, (d) HR-TEM image, (e) SAED pattern, (f) XRD pattern, and (g) elemental mapping images.

In addition, the cross-sectional FE-SEM illustrated in the inset of Fig. S2a, and the high-resolution FE-SEM shown in Fig. S2b reveal a more shrunken fibrous structure with an average diameter of 400 nm by higher carbonization temperature, consisting of uniformly distributed mesopores throughout the length of the fibers. However, the EA result of P-N-C-1200 NFs shows a reduced N content (3.1 wt%) compared to P-N-C-800 (12.1 wt%) and P-N-C-1000 NFs (4.7 wt%). This is because the excessively high carbonization temperature of 1200 ℃ caused the removal of the N dopant in the hollow N-C nanocages, promoting the formation of hollow nanocages composed only of C. The XRD patterns shown in Fig. S2c also shows two broad diffraction peaks assigned to the (0 0 2) and (1 0 1) planes of the NGC material in the NFs, identical to those of the P-N-C-1000 NFs (Fig. 3f), confirming the formation of hierarchical P-N-C-1200 NFs.

Additionally, Raman spectroscopy was performed to confirm the effect of various carbonization temperatures such as 800, 1000, and 1200 ℃ on the crystallinity of carbon matrix in P-N-C NFs (Fig. 4a). All the three samples (i.e., P-N-C-800, P-N-C-1000, and P-N-C-1200 NFs) exhibit a typical Raman signature with the D- and G-band centered at 1344 and 1582 cm^{-1}, respectively [25,26]. However, the area integral intensity ratio (i.e., I_D/I_G) values obtained by the fitting of separate Gaussian curves of two bands, which is typically considered as a critical parameter to inspect the crystalline nature of the carbon outcomes vary significantly for all the three samples. For instance, the I_D/I_G ratio of P-N-C-800 NFs is 2.26 specifying that the sample is amorphous in nature, whereas the I_D/I_G ratio subsequently decreased to 1.69, and 1.58 in case of P-N-C-1000, and P-N-C-1200 NFs demonstrating the formation of the GC with increase in carbonization temperature [27,28]. The reduction in I_D/I_G ratio with increase in carbonization temperature also signifies a lower degree of defects or disordered arrangement in the as-prepared samples because of the availability of soft carbon from the PAN carbonization, which consequently affects the increase of GC occupancy in the composite fibers. In addition, as shown in the EA results (Table S1), the removal of the N-dopant due to the increase in carbonization temperature may also have resulted in a decrease in the I_D/I_G ratio. The graphitic properties of all three P-N-C NFs were once again confirmed through the shift in the combustion temperature region obtained from TG analysis in an air atmosphere. The TGA profiles of all three samples revealed one weight loss step corresponding to combustion of the GC and hollow N-C nanocages as shown in Fig. 4b and c. However, what is noteworthy is that the TGA results of P-N-C-800, P-N-C-1000 and P-N-C-1200 NFs show different weight loss step in the temperature regions of 408–583, 478–625 and 487–650 ℃, respectively. Increasing the carbonization temperature improves the crystallinity of carbon, which makes it difficult to break bonds between carbons resulting in an increase in the combustion temperature of carbon. Further, the total carbon content of P-N-C-800, P-N-C-1000, and P-N-C-1200 composite NFs estimated to be 79, 96, and 97 wt%, respectively, which are in line with the sum of the N and C content obtained from the EA analysis (Table S1). The 13 wt% residual impurity identified only in the TGA results of P-N-C-800 NFs is expected to be ZnO resulting from metallic Zn remaining due to insufficient temperature.

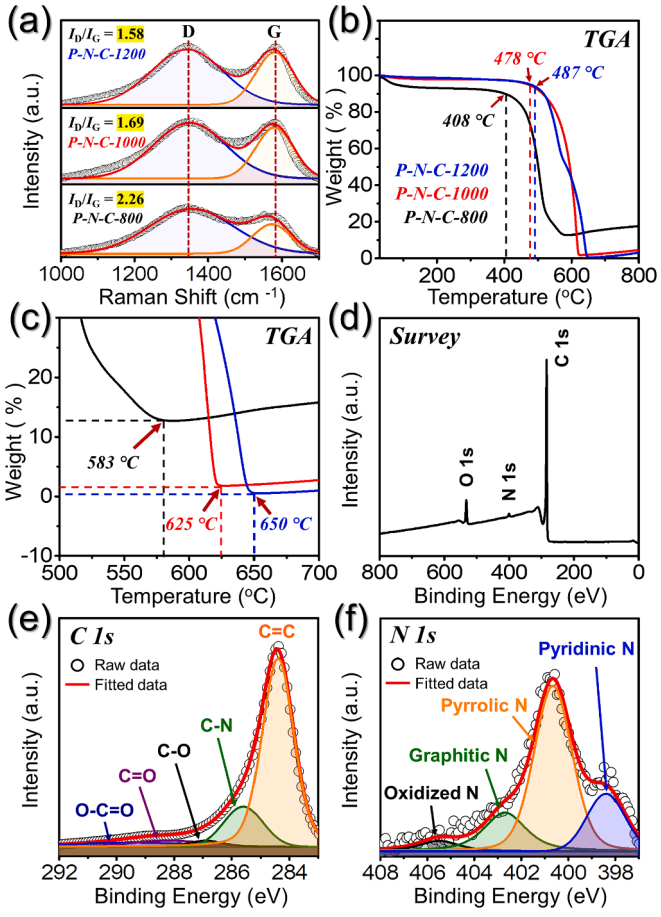

Fig. 4. (a) Fitted Raman spectra obtained using area integrated intensity ratio, and (b,c) TG curves of P-N-C-800, P-N-C-1000, P-N-C-1200 NFs; (d) XPS survey spectrum, and (e,f) core-level XPS spectra of P-N-C-1000 NFs: (e) C 1 *s*, and (f) N 1 *s*.

Besides, based on the TEM, Raman and TGA results described above, P-N-C-1000 NFs comprising only NGC matrix and hollow N-C nanocages were selected as the optimized P-N-C NFs, and XPS studies were performed to investigate the chemical composition and electronic structure of P-N-C-1000 NFs. Fig. 4d shows the high resolution XPS survey scan of C 1 *s*, N 1 *s*, and O 1 *s* core levels of P-N-C-1000 NFs. The high-resolution XPS spectra of C 1 *s* shown in Fig. 4e displays five well-separated peaks at binding energy of 284.4, 285.6, 287.0, 288.3, and 290.6 eV, which are in accordance with the characteristic peaks of C = C, C–N, C–O, C = O, and O–C = O, respectively [5,29]. The strong peaks observed at the binding energy of 284.4, and 285.6 eV for C = C along with C–N suggest the presence of carbonaceous material along with N-doping to form NGC skeleton [30,31]. Moreover, the deconvoluted N 1 *s* XPS spectra displayed in Fig. 4f reveal four peaks located at binding energy of 398.2, 400.7, 402.7, and 405.6 eV, which correspond to pyridinic-N, pyrrolic-N, graphitic-N, and oxidized-N species, respectively, validating the doping of N in the carbon network [32,33]. To confirm the pore characteristics of P-N-C NFs containing hollow N-C nanocages, adsorption–desorption isotherms are achieved for the P-N-C-800, P-N-C-1000, and P-N-C-1200 NFs using N_2 gas as the adsorbate, as displayed in Fig. S3 and Fig. S4. N_2 adsorption–desorption isotherms of all the three NFs (Fig. S3a, S3c, and S4a) shows the type IV isotherm with distinct broad hysteresis loop observed within the pressure range of 0.0–1.0P/P_0. The P-N-C-800 NFs (Fig. S3a) exhibits a high BET surface area of 292 m^2/g^{-1} resulting from the micro- and mesopores in the composite NFs. Furthermore, the BJH desorption pore-size distribution plot displayed in Fig. S3b validates the presence of micro- and mesopores with a y-value peaked at 1.1 and 31 nm. Micropores initiated from N-species derived from PAN and 2-methylimidazole which influence the surface defects. Besides, the mesopores are attributed hollow N-C nanocages formed to the thermal decomposition ZIF-8 polyhedra. Similarly, P-N-C-1000 and P-N-C-1200 NFs display BET surface areas of 199 and 133 m^2/g^{-1} shown in Fig. S4a and Fig. S3c, respectively, and it was observed that the specific surface area decreased with increasing carbonization temperature. The BJH desorption pore size distribution plots of P-N-C-1000 shown in Fig. S4b reveals distinct peaks corresponding to the micropores (1.2 nm) and mesopores (33 nm). Likewise, P-N-C-1200 NFs shown in Fig. S3d also exhibit well-distinguished peaks centered at 1.3 nm for micropores and 37 nm for mesopores. It is noteworthy to mention that the micropore intensity decreases for P-N-C-1000 and P-N-C-1200 compared to P-N-C-800 NFs, suggesting that the increase in

carbonization temperature resulted in the more graphitization of the carbon matrix and the extinction of micropores by N-species in the ZIF-8 derived hollow N-C nanocages, resulting in a lower BET surface area. These observations are consistent with the Raman (Fig. 4a) and EA analysis results (Table S1). Additionally, to confirm the micropores of P-N-C NFs in detail, micropore distribution analysis was performed as a representative of P-N-C-1000 NFs, as shown in Fig. S4c. Therefore, the Raman, XPS, and BET results suggest that the temperature of carbonization has a great influence on characteristics of P-N-C NFs, such as graphitic nature, N-species content, and microporosities, which should be optimized as an electrode material.

To validate the electrochemical advantages of hollow N-C nanocages within P-N-C NFs, non-porous N-C NFs derived from PAN (PAN-C NFs) in the absence of ZIF-8 polyhedra were also prepared. The overall characteristic of PAN-C NFs obtained by the same carbonization condition with P-N-C-1000 NFs detailly was discussed in Fig. S5. FE-SEM images of PAN-C NFs (Fig. S5a and b) reveal dense and smooth 1D fibrous morphologies with an average diameter of 200 nm due to the absence of ZIF-8 polyhedra. In addition, the high-resolution FE-SEM image observed in Fig. S5b confirms the formation of non-porous NFs with high-density. The XRD pattern (Fig. S5c) illustrates two broad diffraction peaks located at 22° and 44°, which agree well with those of P-N-C NFs for PAN-derived GC materials. Moreover, the result of Raman spectroscopy (Fig. S5d) shows shows an area integral intensity-based I_D/I_G value of 1.51, which is lower than that of P-N-C-1000 NFs due to the non-porous nature resulting from the absence of hollow N-C nanocages within PAN-C NFs. The altered thermal properties resulted from non-porous structures are verified through TG analysis of PAN-C NF obtained in an air atmosphere. As shown in Fig. S5e, the TGA profile of PAN-C NFs exhibits one weight loss step by decomposition of GC observed at temperatures above 500 °C. The weight loss finalized at 665 °C indicates that PAN-C NFs have similar thermal stability to P-N-C-1200 NFs due to their non-porous structure despite the lower carbonization temperature. Furthermore, the total C content of PAN-C NFs is estimated to be 97 wt%, which is compatible with sum of the N and C contents obtained from the EA analysis (Table S1). As shown in Table S1,

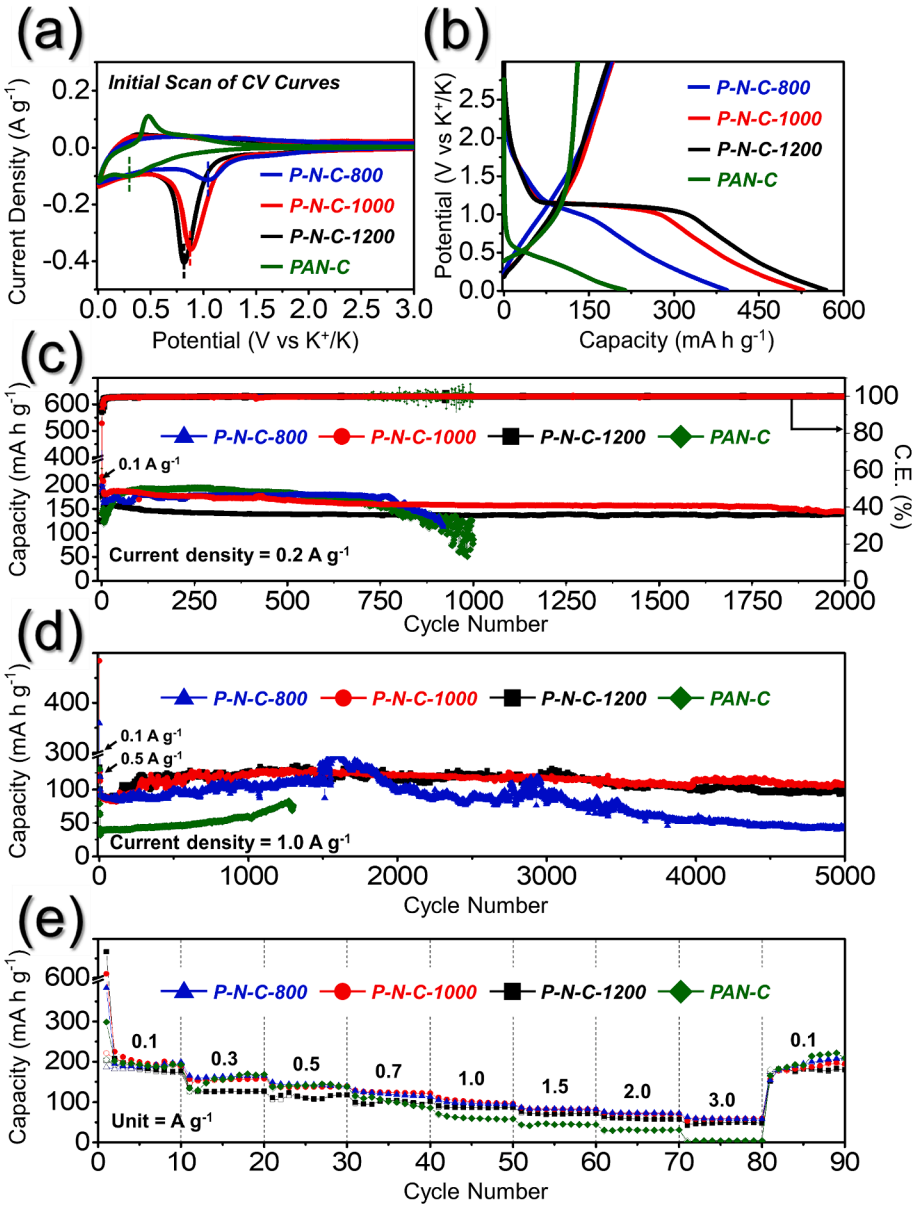

Fig. 5. Electrochemical properties of P-N-C-800, P-N-C-1000, P-N-C-1200, and PAN-C NFs for K-ion storage: (a) initial scan of CV curves, (b) initial discharge/charge curves at current density of 0.1 A g^{-1}, (c) cycle performances at current density of 0.2 A g^{-1}, (d) cycle performances at current density of 1.0 A g^{-1}, and (e) rate performances.

the N content of 3.9 wt% estimated from EA measurements was derived from PAN. Additionally, the N_2 adsorption–desorption isotherm study for the PAN-C NFs displayed in Fig. S5f disclose a lower surface area of 16 m^2/g^{-1} due to the absence of micro and mesopores. Therefore, the above findings suggest that PAN-C NFs with a dense-type morphology that predicts poorer electrochemical properties compared to P-N-C NFs.

Motivated by the intriguing physicochemical properties, the energy storage capabilities of the P-N-C-800, P-N-C-1000, P-N-C-1200, and PAN-C NFs employed as KIB anodes were further explored and are summarized in Fig. 5. The first CV scan shown in Fig. 5a reveals that the P-N-C-800 anode exhibits a broad, low-intensity peak at 1.03 V, attributed to the formation of a solid electrolyte interphase (SEI) film resulting from electrolyte decomposition along with the K-ion adsorption on the electrode surface [34]. However, substantial variations in peak position and intensity are observed during the first cathodic scan for anodes synthesized at higher temperatures i.e., P-N-C-1000 and P-N-C-1200. For instance, the cathodic peak shifts to lower potentials for P-N-C-1000 (0.88 V) and P-N-C-1200 (0.82 V) anodes with concomitant increase in peak intensity. The cathodic peak shifts are due to the fact that the specific surface areas for P-N-C-1000 (199 m^2/g^{-1}) and P-N-C-1200 (133 m^2/g^{-1}) are lower than that of the P-N-C-800 (292 m^2/g^{-1}) anodes. As mentioned above, the shift in cathode peak to lower potentials surprisingly follow the specific surface area trend, which decreases in the order of P-N-C-800, P-N-C-1000, and P-N-C-1200 NFs, with the cathodic peak shifted to the lowest potential (0.30 V) for the non-porous PAN-C anode. Notably, the high cathodic current intensities for P-N-C-1000 and P-N-C-1200 anodes are attributed to relatively higher graphitic nature within the nanostructure, which resulted in improved redox kinetics during the first cycle. Additionally, the cathodic peak at approximately 0.02 V for all synthesized anodes is linked to K-ion intercalation into the GC layer [35]. During the reverse scan, a broad anodic peak at approximately 0.35 V for P-N-C-800, P-N-C-1000, and P-N-C-1200 anodes signifies K-ion deintercalation from the GC layer [36,37]. Another anodic peak at 1.33 V corresponds to K-ion desorption from the electrode surface. Importantly, the low intensities of anodic peaks for P-N-C-800, P-N-C-1000, and P-N-C-1200 anodes, suggest substantial irreversible capacity loss during the first scan. In contrast, the anodic peak at 0.47 V for PAN-C anode exhibits comparable intensity to the respective cathodic peak, indicating high redox process reversibility, especially during the first cycle. Subsequent cycles (Fig. S6) show overlapping CV curves for all synthesized NFs, indicating a reversible redox mechanism. Overall, the CV curves underscore that NFs prepared at high temperature i.e., P-N-C-1000 and P-N-C-1200, exhibits superior redox kinetics compared to the sample prepared at low temperature (P-N-C-800), mainly due to a high degree of graphitization facilitating faster redox processes.

To verify the redox behavior revealed by CV, initial galvanostatic charge–discharge (GCD) curves were recorded at a current density of 0.1 A g^{-1} for all anodes, as shown in Fig. 5b. During discharge, the P-N-C-800 anode exhibited a brief, erratic voltage plateau around 1.1 V, in contrast to the P-N-C-1000 and P-N-C-1200 anodes, which demonstrated more prolonged, flat voltage plateaus. The extended voltage plateaus during discharge for P-N-C-1000 and P-N-C-1200 anodes correlated well with high cathodic current intensities observed in the CV plots. Conversely, the PAN-C anode revealed a short and indistinct discharge voltage plateau at approximately 0.5 V. These observations strongly suggest superior redox activities within P-N-C-1000 and P-N-C-1200 anodes compared to P-N-C-800 and PAN-C. Throughout the charge process, all anodes revealed a similar redox process with no distinct charge voltage plateaus. Correspondingly, the P-N-C-800, P-N-C-1000, P-N-C-1200, and PAN-C electrodes exhibited a charge/discharge capacity of 190/394, 192/529, 184/569, and 130/214 mA h g^{-1}, respectively, along with an initial coulombic efficiencies (ICE) of 48, 36, 33, and 61 %, respectively. It is noteworthy that the irreversible capacity loss typically diminishes with a reduction in sample porosity [38]. Among all the prepared samples, PAN-C anode exhibited the lowest surface area (16 m^2/g^{-1}), a staggering 95 % lower than the highest porous sample (i.e., P-N-C-800), resulting in the highest ICE value. Besides, the increase in pyrolysis temperature led to a concurrent decrease in surface area and defects due to an increase in degree of graphitization [39]. Among all ZIF-8-derived porous NFs, the P-N-C-1200 anode exhibited the lowest surface area, mainly due to a minimal number of defects in the carbonaceous framework, as evidenced by the BJH pore size distribution in Fig. S3d. However, a surface area value of 133 m^2/g^{-1} (Fig. S3c) is attributed to the existence of hollow C nanocage derived mesopores. The minimized defect number and high graphitic nature (Fig. 4a) of P-N-C-1200 NFs resulted in the sluggish diffusion kinetics of K-ion, which led to the deposition of highly reactive metallic-K on the surface during the potassiation process [40–42]. Moreover, the hollow C nanocage-derived mesopores provided a large contact area with the electrolyte, leading to a higher proportions of irreversible side reactions and gradual decomposition of electrolyte. This resulted in subsequent SEI formation on the sample surface due to the deposited metallic-K, which contributed to the low ICE or high irreversible capacity loss of P-N-C-1200 NFs [43]. Similar inferences could be drawn for P-N-C-1000 NFs. Nevertheless, the lower ICE results in stable SEI formation, essential for prolonged cycling stability and high coulombic efficiency approaching 100 % after numerous cycles. Moreover, the ICE values of P-N-C NFs are compared to the other carbon-based anodes reported previously for K-ion batteries in Table S2.

Cycling stability is another crucial parameter for any battery material for its wide scale application. The prepared NFs were tested for cycling stability performance at the current density of 0.2 and 1.0 A g^{-1} with high areal loading mass (1.8–1.9 mg cm^{-2}) of the active material, as shown in Fig. 5c and d, respectively. Initially, an activation process was performed for all anodes by achieving GCD at a low current density of 0.1 A g^{-1} for five cycles. As evident from Fig. S7a, P-N-C-800, P-N-C-1000, and P-N-C-1200 anodes exhibits stable discharge capacity values during initial 100 cycles, mainly due to porous and conductive carbonaceous framework. Conversely, for PAN-C anode, the discharge capacities increases monotonically till 60 cycles, owing to the continuous activation process, which arises due to the non-porous structure of the anode. Notably, the initial discharge capacities for P-N-C-1000 and P-N-C-1200 anodes were observed to be 181 and 153 mA h g^{-1}, respectively, which stabilized to 145 (80 % retention), and 139 (91 % retention) mA h g^{-1} after 2000 continuous discharge/charge cycles (Fig. 5c) despite the high areal loading mass of 1.8–1.9 mg cm^{-2}. The superior capacity retention is attributed to the highly conductive and interconnected porous structure, which not only alleviate the volume changes effectively during the redox processes but also provide numerous conductive pathways for rapid charge transfer. Besides, high CE values of 99.9 % indicates high reversible redox processes within the cells. In contrast, the cells featuring P-N-C-800 and PAN-C anodes demonstrate poor capacity retention during cycling or cell short-circuiting issues, suggesting poor reliability of the anodes for prolonged cycling. Likewise, similar capacity trends were observed for the prepared NFs when cycled at a higher current density of 1.0 A g^{-1} for longer cycling stability up to 5000 cycles (Fig. 5d). However, it was observed that the capacity increase monotonically till a few hundred cycles, associated with the SEI formation and expanding lattice fringe of GC during repeated cycling. This induces structural defects in the crystal structure, which facilitates more insertion and/or extraction of the K-ions, as discussed previously [44]. Notably, even after prolonged cycling, the P-N-C-1000 and P-N-C-1200 electrodes exhibits higher capacity retention of 96 % (108 mA h g^{-1}) and 81 % (96 mA h g^{-1}), respectively, after 5000th cycle, compared to P-N-C-800 and PAN-C anodes. However, the excessive porous nature and lack of NGC matrix for P-N-C-800 composite NFs subsequently leading to poor capacity retention and substandard cycling properties. These interpretations are more noticeable from the fact that the capacity retention decreased to 37 % (44 mA h g^{-1}) even after 5000 cycles for the P-N-C-800 composite NFs. The cell featuring the PAN-C NFs stopped working after 1295 cycle owing to the excessive decomposition of electrolyte, resulted in thick layer of redox inactive products (as

discussed later). The over-whelming cycling stability of P-N-C-1000 composite NFs even after 10,000 cycles (Fig. S7b) despite the harsh conditions of a high active material loading mass of 1.8–1.9 mg cm^{-2} could be attributed to the several structural benefits. For instance, the porous structure allowed smooth K-ion diffusion due to the improved electrode wetting or electrolyte percolation. Besides, the NGC matrix and N-rich organic linker-derived conductive N-C nanocage accelerated the fast charge transfer during the electrochemical processes by improving the electrical conductivity.

The rate performance of all samples was carried out at various current densities ranging from 0.1 to 3.0 A g^{-1} and the results are displayed in Fig. 5e. In the case of P-N-C-1000 NFs, capacities of 191, 158, 140, 123, 97, 82, 71, and 60 mA h g^{-1} were recorded at the current density of 0.1, 0.3, 0.5, 0.7, 1.0, 1.5, 2.0, and 3.0 A g^{-1}, respectively, at 10th cycle of each current densities. When the current density returned to 0.1 A g^{-1}, the capacity was well recovered to 195 mA h g^{-1} suggesting the remarkable capacity retention and rate capability of P-N-C-1000 NFs. In contrast, the capacities of P-N-C-800/P-N-C-1200/PAN-C electrodes diminish from 199/177/192, 165/128/169, 140/119/139, 115/102/86, 95/87/58, 83/73/44, 73/58/31, and 59/48/4 mA h g^{-1}, respectively, at current densities of 0.1, 0.3, 0.5, 0.7, 1.0, 1.5, 2.0, and 3.0 A g^{-1}. Nevertheless, the PAN-C NFs exhibit poor rate performance, especially at high current densities (1.0–3.0 A g^{-1}) due to the non-porous or dense fibrous structure. The stable rate performance of the P-N-C-1000 NFs validated its structural merits as an advanced anode for KIBs compared to the P-N-C-800, P-N-C-1200, and PAN-C. The porosity within the architecture guarantees improved electrode wetting, facilitating smooth redox processes during the electrochemical testing due to efficient K-ion diffusion. Besides, the synergetic effects of the N-doping, and optimized NGC improved the electrical conductivity of the anode, prompted the rapid transfer of electron/ions by enhancing the electrical contact among various active sites of the electrode. From these observations, P-N-C-1000 NFs exhibited ultra-long cycling stability, indicating long-lasting advanced anodes for effective K-ion storage. Additionally, the electrochemical performance of P-N-C-1000 NFs prepared in the present study is compared with other previously reported carbon-based anodes in the Table S3. Moreover, to explore the potential of P-N-C-1000 anode for practical use, it was combined with P3-type $K_{0.5}(Mn_{0.8}Co_{0.1}Ni_{0.1})O_2$ cathode prepared from co-precipitation approach and two-step heat treatment under air atmosphere for preparation of K-ion full cell, and the relevant information is provided in Fig. S8 and S9. The obtained electrochemical performance of full cell is comparable to the previous reports based on the different cathode and anode systems [45–47].

To better understand the redox properties within the cell, the CV curves were plotted for P-N-C-1000 NFs in the voltage window of 0.01–3.0 V at various sweep rates ranging from 0.1 to 2.0 mV s^{-1} as shown in Fig. 6a. Subsequently, the graphs were plotted between the peak current (i) and scan rates (ν) during reduction/oxidation using the power law equation to distinguish the capacitive and diffusion-controlled mechanisms in the CV curves [29,48].

$$i = av^b \tag{1}$$

$$log(i) = blog(v) + log(a) \tag{2}$$

Here, the a and b variables decide whether the mechanism is capacitive-controlled, or diffusion-controlled. The redox process is mainly diffusion controlled when b value approaches 0.5 whereas capacitive controlled when b value reaches to 1 [6,49,50]. The b values were determined using the slope of log (i) vs. log (ν) plots for various anodic and cathodic peaks. The calculated b values for the various redox peaks of the samples are shown in Fig. 6b and Fig. S10. The b values for three different redox peaks in the P-N-C-1000 NFs were 0.95, 0.88, and 0.90, demonstrating a capacitive dominant mechanism. Likewise, the b values for P-N-C-800 NFs (Fig. S10a and b) were 0.94, 0.89, and 0.81, indicating capacitive

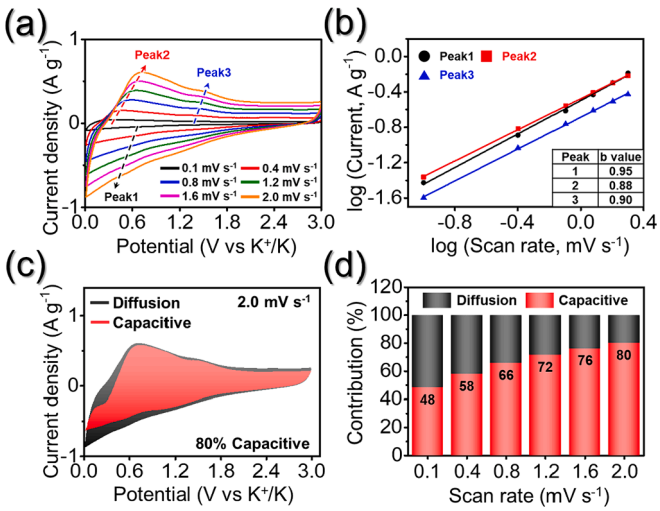

Fig. 6. (a-d) Electrochemical reaction dynamics analysis of the P-N-C-1000 NFs: (a) CV curves obtained at various scan rates, (b) current response (i) versus scan rate (n) at each redox peak, (c) CV curves with the capacitive fraction shown by the red region at a scan rate of 2.0 mV s^{-1}, and (d) bar charts showing the percentage of the capacitive contribution at different scan rates. (For interpretation of the references to colour in this figure legend, the reader is referred to the web version of this article.)

dominant mechanism similar to P-N-C-1000 NFs due to the availability of rich pseudocapacitive reaction sites originating from the high porosity. In contrast, the reaction kinetics for P-N-C-1200 NFs demonstrate lower b values implying a marginally lower capacitive-controlled mechanism (Fig. S10c and d). This is attributed to the lower specific surface area and more graphitic nature dominated by the diffusion-controlled reaction due to higher temperature carbonization. Furthermore, the PAN-C NFs exhibit low b values, indicating that diffusion-controlled reactions dominate the redox processes relatively more than the P-N-C-800 and P-N-C-1000 NFs due to their non-porous nature (Fig. S10e and f). Generally, the capacitive effect of the electrode material is closely related to the reaction kinetics, implying that the transport kinetics is enhanced when the percentage of the capacitive-controlled process is higher. Therefore, the total stored charge in the electrode material was separated into diffusion and capacitive-controlled processes for the quantitative analysis of the capacity contribution to the current response using the following equation [51,52]:

$$i = k_1 v + k_2 v^{1/2} \tag{3}$$

where $k_1\nu$ and $k_2\nu^{1/2}$ are the capacitive and diffusion contributions, respectively, while k_1 and k_2 are the constants obtained from the slope and intercept of the $i(V)/\nu^{1/2}$ versus $\nu^{1/2}$ plot, respectively [25,53]. As shown in Fig. 6c, the capacitive contribution factor ($k_1\nu$) for the P-N-C-1000 NFs, highlighted by the red region, is 80 % at a sweep rate of 2.0 mV s^{-1}. A relatively high capacitive contribution was observed for the P-N-C-1000 NFs at all sweep rates shown in Fig. 6d. Similarly, the surface-controlled reaction contributions in P-N-C-800 NFs demonstrate 76 % of the capacitive process at a sweep rate of 2.0 mV s^{-1} (Fig. S11a and b). In contrast, the P-N-C-1200 and PAN-C NFs shown in Fig. S11c–f reveals low capacitive processes at various sweep rates. These results confirm the kinetically favored rapid K-ion transport for P-N-C-1000 NFs owing to the improved electrolyte percolation within the porous structure and synergetic effect of optimized NGC that facilitate rapid charge transfer.

The superior K-ion storage capability of P-N-C-1000 NFs in comparison to those of P-N-C-800, P-N-C-1200, and PAN-C NFs were further verified by the help of EIS measurements of the cell as shown in Fig. 7. The EIS plots of the electrode materials were recorded prior to cycling, and after the 5th and 300th cycles at the fully charged condition. The

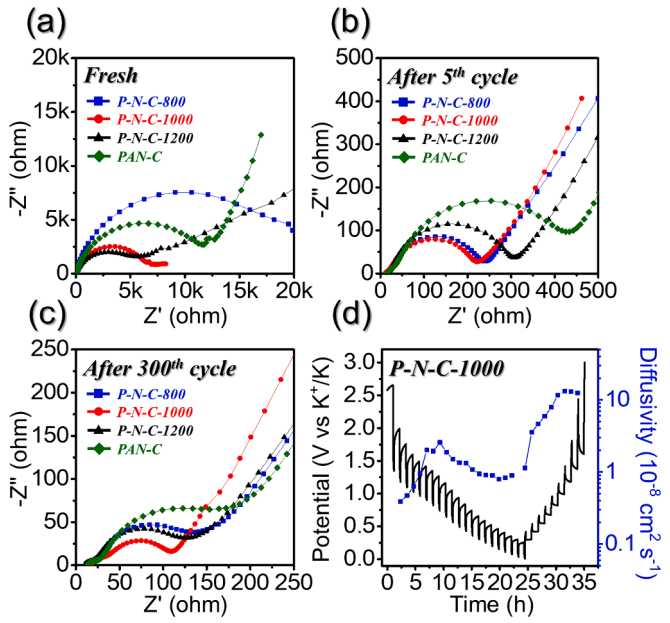

Fig. 7. (a–c) Nyquist impedance plots of assembled cells employed with different anodes during cycling at 0.2 A g^{-1} and (d) GITT curve of P-N-C-1000 NFs: (a) before cycling, (b) after 5th cycle, (c) after 300th cycle, (d) K-ion diffusion coefficient (D_{K^+}) measurement using GITT curve during discharge/charge.

recorded EIS plots were further deconvoluted with the Randle type equivalent circuit model shown in Fig. S12. The charge transfer resistance (R_{ct}) value of P-N-C-800, P-N-C-1000, P-N-C-1200, and PAN-C NFs for the freshly assembled cells were 19.9 k, 6.7 k, 5.7 k, and 11.6 kΩ, respectively as displayed in Fig. 7a and Table S4. The P-N-C NFs exhibited a tendency to have lower R_{ct} values with increasing carbonization temperature. This is attributed to the reduction in porosity and the increase in the fraction of GC with increase in temperature, which enabled the drastic decrease in R_{ct} there by high electrical conductivity was noticed indicating the improved charge transfer kinetics. In contrast, PAN-C NFs showed much higher R_{ct} values than P-N-C-1000 NFs despite having the lowest specific surface area. After the 5th cycle, R_{ct} values of P-N-C-800, P-N-C-1000, P-N-C-1200 NF electrodes decreased due to the formation of SEI film and porous nature of the composite NFs (Fig. 7b). In addition, the PAN-C NFs displayed the highest R_{ct} value among the samples after 5th cycle because of the non-porous nature and low surface area. The EIS plot of the electrodes after 300th cycle is shown in Fig. 7c, where P-N-C-800, P-N-C-1000, P-N-C-1200, and PAN-C NFs exhibited R_{ct} values of 124, 81, 114, and 177 Ω, respectively. These findings imply that the structural merits of P-N-C-1000 NFs not only ensure a kinetically favored electrochemical processes within the cell but also improve the integrity of the electrode during continuous cycling. Since not only the electronic conductivity of nanostructures but also the ionic diffusivity is an important factor for analyzing redox kinetics, the galvanostatic intermittent titration technique (GITT) measurements was employed to calculate the K-ion diffusion coefficients (D_{K^+}) values for P-N-C-800, P-N-C-1000, P-N-C-1200, and PAN-C NFs. The GITT curves for four NFs shown in Fig. 7d and S13 were used to measure the variables required for the calculation, and the D_{K^+} values were measured using the following equation [54]:

$$D_{K^+} = \frac{4}{\pi\tau}\left(\frac{m_b V_M}{M_b S}\right)^2 \left(\frac{\Delta E_s}{\Delta E_\tau}\right)^2 \left(\tau \ll \frac{L^2}{D_{K^+}}\right) \quad (4)$$

Where τ is the current pulse time (600 s), m_b is the mass of active material (0.00277 g), V_M is the molar volume of the active material (42.74 cm^3 mol^{-1}), M_b is the molecular weight of active material (12.01 g mol^{-1}), S is the geometric area of the electrode (1.5386 cm^2), and L is the thickness of the electrodes. ΔE_s is the potential change after every equilibrium process. The determination of ΔE_s and ΔE_τ values is presented in Fig. S14. The D_{K^+} values for P-N-C-800, P-N-C-1000, P-N-C-1200, and PAN-C NFs were calculated approximately 4.3 × 10^{-8}, 3.5 × 10^{-8}, 3.3 × 10^{-8}, and 2.1 × 10^{-8} cm^2 s^{-1}, respectively. The higher D_{K^+} value observed for P-N-C-800 NFs is attributed to the superior porosity which facilitate better diffusion of charged species. However, it is noteworthy to mention that the proportion of GC within the P-N-C-800 NFs is lowest among all the composite NFs, which signifies that the P-N-C-800 NFs possess relatively low electronic conductivity, suspecting that during prolonged cycling the sample might not withstand with improved redox kinetics. This observation matches well with the EIS values shown in Table S4. In contrast, the P-N-C-1000 NFs also demonstrate relatively higher D_{K^+} value, attributed to the highly optimized NGC along with the porous nature, which guarantees kinetically favored redox processes. Moreover, the D_{K^+} values in the present study are in close proximity or higher than the previously reported literatures on various anode materials [55,56].

To investigate the structural stability of the composite NFs, the post-cycling morphologies of P-N-C-800, P-N-C-1000, P-N-C-1200, and PAN-C NFs were examined after 5000 cycles, as revealed in Fig. 8. The P-N-C-1000, and P-N-C-1200 NFs maintained their porous nanofiber structure very well even after repeated discharge/charge cycles at the current density of 1.0 A g^{-1} due to their high structural stability as displayed in Fig. 8b and c, respectively. To validate this hypothesis, we analyzed the changes in thickness of fresh as well as cycled P-N-C-1000 electrode after 5000 cycles. From Fig. S15a–d, it is evident that the thickness of the anode changes marginally from fresh (74 μm) electrode to cycled electrode (84 μm), confirming the structural integrity of the prepared nanostructure. In addition, the P-N-C-800 NFs showed an agglomerated morphology after 5000 cycles due to their weak mechanical strength through the excessive porous nature and lack of NGC matrix (Fig. 8a). Moreover, the surface for PAN-C NFs was covered with thick side-reacted products formed during 5000 cycles by the slow diffusion of K-ions owing to its non-porous nature, resulting in an unrecognizable morphology (Fig. 8d). Therefore, the above results suggest the decent K-

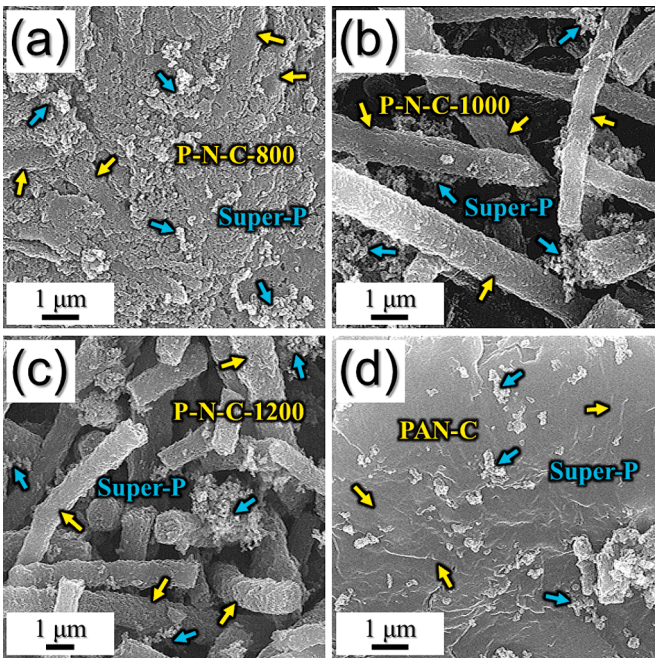

Fig. 8. (a-d) FE-SEM images of the P-N-C-800, P-N-C-1000, P-N-C-1200, and PAN-C NFs obtained after 5000 cycles at 1.0 A g^{-1}: (a) P-N-C-800, (b) P-N-C-1000, (c) P-N-C-1200, and (d) PAN-C NFs.

ion storage properties of the P-N-C-1000, P-N-C-1200 NFs, including remarkable cyclic stability and rate capability and were accredited to the advantages of the unique nanostructures. The unique porous structure and hollow N-C nanocages allowed the efficient penetration of the liquid electrolyte into the electrode and supported rapid electron/ion transfer *via* numerous N-doped conductive pathways. Furthermore, the robust structure based on NGC framework not only provides structural integrity to the composite NFs to prevent it from collapsing during the redox processes but also offers numerous conducting pathways for fast charge transfer kinetics.

4. Conclusions

In this study, an optimized synthesis protocol is followed to develop unique nanostructures comprising of porous and hollow carbon nanocages which are encapsulated within the NGC matrix. The interconnected hollow N-doped C nanocages efficiently alleviated the volume fluctuations and permitted the facile penetration of electrolyte into the nanostructures. The nano sized N-doped C nanocages composited with the GC enabled the faster transfer of electrons leading to rapid reaction kinetics, and the optimized NGC matrix enables reversible K-ion insertion/extraction reactions, conferring structural integrity. In addition to P-N-C-1000 NFs with above advantages, P-N-C-800 NFs with many defects in the carbon matrix, and P-N-C-1200 NF with hollow C nanocages and abundant NGCs were applied as anodes for KIBs and the results were compared. P-N-C-800 NFs showed high discharge capacities at low current density due to numerous defects, while exhibiting poor cyclic stability. P-N-C-1200 NFs displayed excellent structural robustness due to the NGC-rich matrix, but exhibited slightly poor rate performance due to the absence of N-dopants in the nanocage. Finally, the optimized P-N-C-1000 composite NFs could deliver stable cycle performance up to 10,000 cycles even at a high current density of 1.0 A g^{-1} with high areal loading mass of the active material (1.8–1.9 mg cm^{-2}), demonstrating that this approach is advantageous for achieving good electrochemical performance. This approach may pave the way towards the development of composite NFs consisting of hollow N-doped C nanocages composited with conductive NGC matrix towards the various energy-related applications.

CRediT authorship contribution statement

Jae Seob Lee: Writing – review & editing, Writing – original draft, Visualization, Investigation, Formal analysis, Data curation, Conceptualization. **Narasimharao Kitchamsetti:** Writing – review & editing, Writing – original draft, Visualization, Data curation. **Jung Sang Cho:** Writing – review & editing, Supervision, Project administration, Investigation, Funding acquisition, Conceptualization.

Declaration of competing interest

The authors declare that they have no known competing financial interests or personal relationships that could have appeared to influence the work reported in this paper.

Data availability

No data was used for the research described in the article.

Acknowledgments

This work was supported by the National Research Foundation of Korea (NRF) and the Commercialization Promotion Agency for R&D Outcomes (COMPA) funded by the Ministry of Science and ICT (Grant No.: RS-2023-00217581, RS-2023-00304768). This work was partially by results of a study on the "Leaders in INdustry-university Cooperation 3.0" Project, supported by the Ministry of Education and National Research Foundation of Korea.

Appendix A. Supplementary data

Supplementary data to this article can be found online at https://doi.org/10.1016/j.cej.2024.150465.

References

[1] A.K. Nulu, V. Nulu, J.S. Moon, K.Y. Sohn, Unified NCNT@rGO bounded porous silicon composite as an anode material for Lithium-ion batteries, Korean J. Chem. Eng. 38 (2021) 1923–1933, https://doi.org/10.1007/s11814-021-0813-5.
[2] E.H. Lim, J.Y. Chun, C.S. Jo, J.K. Hwang, Recent advances in the synthesis of mesoporous materials and their application to lithium-ion batteries and hybrid supercapacitors, Korean J. Chem. Eng. 38 (2021) 227–247, https://doi.org/10.1007/s11814-020-0693-0.
[3] Y.J. Ha, Y.J. Choi, J.I. Choi, B.K. Park, J.H. Yang, K.J. Kim, Degradation mechanism of polyethylene separators in lithium-ion batteries after prolonged cycling, Korean J. Chem. Eng. 40 (2023) 519–523, https://doi.org/10.1007/s11814-022-1304-z.
[4] Y. Wu, Y. Yao, L.F. Wang, Y. Yu, Recent Progress on modification strategies of alloy-based anode materials for alkali-ion batteries, Chem. Res. Chin. Univ. 37 (2021) 200–209, https://doi.org/10.1007/s40242-021-0001-5.
[5] J.S. Lee, J.S. Park, K.W. Baek, R. Saroha, S.H. Yang, Y.C. Kang, J.S. Cho, Coral-like porous microspheres comprising polydopamine-derived N-doped C-coated $MoSe_2$ nanosheets composited with graphitic carbon as anodes for high-rate sodium- and potassium-ion batteries, Chem. Eng. J. 456 (2023) 141118, https://doi.org/10.1016/j.cej.2022.141118.
[6] J.S. Lee, R. Saroha, J.H. Oh, C.Y. Cho, B. Jin, D.W. Kang, J.S. Cho, Camphene-derived hollow and porous nanofibers decorated with hollow NiO nanospheres and graphitic carbon as anodes for efficient lithium-ion storage, J. Ind. Eng. Chem. 114 (2022) 276–287, https://doi.org/10.1016/j.jiec.2022.07.017.
[7] R. Saroha, J.H. Ahn, J.S. Cho, A short review on dissolved lithium polysulfide catholytes for advanced lithium-sulfur batteries, Korean J. Chem. Eng. 38 (2021) 461–474, https://doi.org/10.1007/s11814-020-0729-5.
[8] X.J. Xu, D.C. Zhang, Z.S. Wang, S.Y. Zuo, J.J. Yuan, R.Z. Hu, J. Liu, Ultrafine ZnS Nanoparticles in the nitrogen-doped Carbon matrix for long-life and high-stable potassium-ion batteries, ACS Appl. Mater. Interfaces 13 (2021) 11007–11017, https://doi.org/10.1021/acsami.0c23136.
[9] S. Dhir, S. Wheeler, I. Capone, M. Pasta, Outlook on K-ion batteries, Chem 6 (2020) 2442–2460, https://doi.org/10.1016/j.chempr.2020.08.012.
[10] D.M. Zhang, Z.W. Chen, J. Bai, C.C. Yang, Q. Jiang, Highly nitrogen-doped porous Carbon nanosheets as high-performance anode for potassium-ion batteries, Batteries Supercaps 3 (2020) 185–193, https://doi.org/10.1002/batt.201900144.
[11] Z.L. Jian, W. Luo, X.L. Ji, Carbon electrodes for K-ion batteries, J. Am. Chem. Soc. 137 (2015) 11566–11569, https://doi.org/10.1021/jacs.5b06809.
[12] L.F. Cui, Z. Wang, S.F. Kang, Y.Y. Fang, Y. Chen, W.K. Gao, Z.Y. Zhang, X. Gao, C. Y. Song, X.D. Chen, Y.G. Wang, G.X. Wang, N, P codoped hollow Carbon nanospheres decorated with $MoSe_2$ ultrathin nanosheets for efficient potassium-ion storage, ACS Appl. Mater. Interfaces 14 (2022) 12551–12561, https://doi.org/10.1021/acsami.1c24989.
[13] F. Wang, Y. Liu, H.J. Wei, T.F. Li, X.H. Xiong, S.Z. Wei, F.Z. Ren, A.A. Volinsky, Recent advances and perspective in metal coordination materials-based electrode materials for potassium-ion batteries, Rare Metals 40 (2021) 448–470, https://doi.org/10.1007/s12598-020-01649-1.
[14] B. Wang, Y. Peng, F. Yuan, Q. Liu, L.Z. Sun, P. Zhang, Q.J. Wang, Z.J. Li, Y.A. Wu, A comprehensive review of carbons anode for potassium-ion battery: fast kinetic, structure stability and electrochemical, J. Power Sources 484 (2021) 229244, https://doi.org/10.1016/j.jpowsour.2020.229244.
[15] Q.Y. Xie, H. Ou, Q.Y. Yang, X.M. Lin, A. Zeb, K. Li, X.L. Chen, G.Z. Ma, A review on metal-organic framework-derived anode materials for potassium-ion batteries, Dalton Trans. 50 (2021) 9669–9684, https://doi.org/10.1039/D1DT01482J.
[16] Y.R. Lee, J. Kim, W.S. Ahn, Synthesis of metal-organic frameworks: a mini review, Korean J. Chem. Eng. 30 (2013) 1667–1680, https://doi.org/10.1007/s11814-013-0140-6.
[17] X.F. Zhou, L.L. Chen, W.H. Zhang, J.W. Wang, Z.J. Liu, S.F. Zeng, R. Xu, Y. Wu, S. F. Ye, Y.Z. Feng, X.L. Cheng, Z.Q. Peng, X.F. Li, Y. Yu, Three-dimensional ordered macroporous metal-organic framework single crystal-derived nitrogen-doped Hierarchical porous Carbon for high-performance potassium-ion batteries, Nano Lett. 19 (2019) 4965–4973, https://doi.org/10.1021/acs.nanolett.9b01127.
[18] D.K. Kim, J.S. Byun, S. Moon, J.Y. Choi, J.H. Chang, J.D. Suk, Molten salts approach of metal-organic framework-derived nitrogen-doped porous carbon as sulfur host for lithium-sulfur batteries, Chem. Eng. J. 441 (2022) 135945, https://doi.org/10.1016/j.cej.2022.135945.
[19] J.L. Yang, Z.C. Ju, Y. Jiang, Z. Xing, B.J. Xi, J.K. Feng, S.L. Xiong, Enhanced capacity and rate capability of nitrogen/oxygen dual-doped Hard Carbon in capacitive potassium-ion storage, Adv. Mater. 30 (2018) 1700104, https://doi.org/10.1002/adma.201700104.
[20] B.L. Rui, J.H. Li, L.M. Chang, H.R. Wang, L. Lin, Y. Guo, P. Nie, Engineering MoS_2 nanosheets anchored on metal organic frameworks derived carbon polyhedra for superior lithium and potassium storage, Front. Energy Res. 7 (2019) 142, https://doi.org/10.3389/fenrg.2019.00142.

[21] R. Saroha, J.H. Oh, Y.H. Seon, Y.C. Kang, J.S. Lee, D.W. Jeong, J.S. Cho, Freestanding interlayers for li-S batteries: design and synthesis of hierarchically porous N-doped C nanofibers comprising vanadium nitride quantum dots and MOF-derived hollow N-doped C nanocages, J. Mater. Chem. A 9 (2021) 11651–11664, https://doi.org/10.1039/D1TA01802G.

[22] N. Davoodian, A.N. Pour, M. Izadyar, A. Mohammadi, A. Salimi, S.M.K. Shahri, Fischer-tropsch synthesis using zeolitic imidazolate framework (ZIF-7 and ZIF-8)-supported cobalt catalysts, Appl. Organomet. Chem. 34 (2020) e5747.

[23] Y.Y. Zhang, Y. Jia, M. Li, L. Hou, Influence of the 2-methylimidazole/zinc nitrate hexahydrate molar ratio on the synthesis of zeolitic imidazolate framework-8 crystals at room temperature, Sci. Rep. 8 (2018) 9597, https://doi.org/10.1038/s41598-018-28015-7.

[24] Y.H. Seon, R. Saroha, J.S. Cho, Hierarchically porous N-doped C nanofibers comprising TiO_2 quantum dots and ZIF-8-derived hollow C nanocages as ultralight interlayer for stable li-S batteries, Compos. Part B-Eng. 237 (2022) 109856, https://doi.org/10.1016/j.compositesb.2022.109856.

[25] J.S. Lee, R. Saroha, S.H. Oh, D.H. Shin, S.M. Jeong, J.K. Kim, J.S. Cho, Rational Design of Perforated Bimetallic (ni, mo) Sulfides/N-doped graphitic Carbon composite microspheres as anode materials for Superior na-ion batteries, Small Methods 5 (2021) 2100195, https://doi.org/10.1002/smtd.202100195.

[26] S.H. Oh, M.S. Jo, S.M. Jeong, Y.C. Kang, J.S. Cho, Hierarchical yolk-shell CNT-(NiCo)O/C microspheres prepared by one-pot spray pyrolysis as anodes in lithium-ion batteries, Chem. Eng. J. 368 (2019) 438–447, https://doi.org/10.1016/j.cej.2019.02.144.

[27] M.S. Jo, J.S. Lee, S.Y. Jeong, J.K. Kim, Y.C. Kang, D.W. Kang, S.M. Jeong, J.S. Cho, Golden bristlegrass-like Hierarchical graphene nanofibers entangled with N-doped CNTs containing $CoSe_2$ nanocrystals at each node as anodes for high-rate sodium-ion batteries, Small 16 (2020) 2003391, https://doi.org/10.1002/smll.202003391.

[28] J.D. Zhu, Z. Gao, M. Kowalik, K. Joshi, C.M. Ashraf, M.I. Arefev, Y. Schwab, C. Bumgardner, K. Brown, D.E. Burden, L.W. Zhang, J.W. Klett, L.V. Zhigilei, A.C. T. van Duin, X.D. Li, Unveiling Carbon ring structure formation mechanisms in polyacrylonitrile-derived Carbon fibers, ACS Appl. Mater. Interfaces 11 (2019) 42288–42297, https://doi.org/10.1021/acsami.9b15833.

[29] C.S. Kim, R. Saroha, H.H. Choi, J.H. Oh, G.D. Park, D.W. Kang, J.S. Cho, High-performance cathode promoted by reduced graphene oxide nanofibers with well-defined interconnected meso-/micro pores for rechargeable li-se batteries, J. Ind. Eng. Chem. 121 (2023) 489–498, https://doi.org/10.1016/j.jiec.2023.02.004.

[30] J.M. Choi, R. Saroha, J.S. Kim, M.R. Jang, J.S. Cho, Porous nanofibers comprising VN nanodots and densified N-doped CNTs as redox-active interlayers for li-S batteries, J. Power Sources 559 (2023) 232632, https://doi.org/10.1016/j.jpowsour.2023.232632.

[31] N. Kitchamsetti, D. Kim, High performance hybrid supercapacitor based on hierarchical MOF derived $CoFe_2O_4$ and $NiMn_2O_4$ composite for efficient energy storage, J. Alloy. Compd. 959 (2023) 170483, https://doi.org/10.1016/j.jallcom.2023.170483.

[32] J.M. Choi, J.S. Lee, J.S. Cho, One-pot synthesis strategy of sea urchin-like hollow microspheres comprising MoO_x nanorods attached via N-doped C as anodes for lithium-ion batteries, Chem. Eng. J. 439 (2022) 135536, https://doi.org/10.1016/j.cej.2022.135536.

[33] J.S. Cho, J.K. Lee, Y.C. Kang, Graphitic Carbon-coated $FeSe_2$ hollow nanosphere-decorated reduced graphene oxide hybrid nanofibers as an efficient anode material for sodium ion batteries, Sci. Rep. 6 (2016) 23699, https://doi.org/10.1038/srep23699.

[34] G.J. Zheng, Z. Xing, X.R. Gao, C.H. Nie, Z.H. Xu, Z.C. Ju, Fabrication of 2D cu-BDC MOF and its derived porous carbon as anode material for high-performance Li/K-ion batteries, Appl. Surf. Sci. 559 (2021) 149701, https://doi.org/10.1016/j.apsusc.2021.149701.

[35] X.D. Li, J.L. Li, L. Ma, C.Y. Yu, Z. Ji, L.K. Pan, W.J. Mai, Graphite anode for potassium ion batteries: current status and perspective, Energy Environ. Mater. 5 (2022) 458–469, https://doi.org/10.1002/eem2.12194.

[36] P. Li, H. Kim, K.H. Kim, J.K. Kim, H.G. Jung, Y.K. Sun, State-of-the-art anodes of potassium-ion batteries: synthesis, chemistry, and applications, Chem. Sci. 12 (2021) 7623–7655, https://doi.org/10.1039/D0SC06894B.

[37] C.C. Zhang, H.G. Pan, L.X. Sun, F. Xu, Y.F. Ouyang, F. Rosei, Progress and perspectives of 2D materials as anodes for potassium-ion batteries, Energy Storage Mater. 38 (2021) 354–378, https://doi.org/10.1016/j.ensm.2021.03.007.

[38] L. Xiao, H. Lu, Y. Fang, M.L. Sushko, Y. Cao, X. Ai, H. Yang, J. Liu, Low-defect and low-porosity hard carbon with high coulombic efficiency and high capacity for practical sodium ion battery anode, Adv. Energy Mater. 8 (2018) 1703238, https://doi.org/10.1002/aenm.201703238.

[39] Y. Tzeng, C.-Y. Jhan, Y.-H. Wu, Effects of pyrolysis on high-capacity si-based anode of lithium ion battery with high coulombic efficiency and long cycling life, Nanomaterials 12 (2022) 469–486, https://doi.org/10.3390/nano12030469.

[40] A.J. Naylor, M. Carboni, M. Valvo, R. Younesi, interfacial reaction mechanisms on graphite anodes for K-ion batteries, ACS Appl. Mater. Interfaces 11 (2019) 45636–45645, https://doi.org/10.1021/acsami.9b15453.

[41] Y. Lei, S. Zhang, J. Dong, Y. Gao, C.W. Gao, Y.J. Wei, L. Qin, D. Han, D.Q. Huang, G.D. Wei, D.Y. Zhai, F.Y. Kang, Potassium-enriched graphite for use as stable hybrid anodes in high-efficiency potassium batteries, Carbon 201 (2023) 1030–1037, https://doi.org/10.1016/j.carbon.2022.09.088.

[42] K.K. Xiao, J.F. Wu, H.H. Yan, Y. Mo, W. Zhou, Y.F. Peng, S. Chen, X.Y. Cui, L. Chen, C.H. Xu, J.L. Liu, Intercalation-deposition mechanism induced by aligned carbon fiber toward dendrite-free metallic potassium batteries, Energy Storage Mater. 51 (2022) 122–129, https://doi.org/10.1016/j.ensm.2022.06.033.

[43] X. Zhao, Y. Chen, H. Sun, T. Yuan, Y. Gong, X. Liu, T. Chen, Impact of surface structure on SEI for carbon materials in alkali ion batteries: a review, Batteries 9 (2023) 226–243, https://doi.org/10.3390/batteries9040226.

[44] J.S. Lee, H.S. Ka, R. Saroha, Y.C. Kang, D.-W. Kang, J.S. Cho, Three-dimensional hierarchically porous micro sponge-ball comprising anatase TiO_2 nanodots and N-doped graphitic C as anodes for ultra-stable li-ion batteries, J. Energy Storage 66 (2023) 107396, https://doi.org/10.1016/j.est.2023.107396.

[45] C. Lv, W. Xu, H. Liu, L. Zhang, S. Chen, X. Yang, X. Xu, D. Yang, 3D sulfur and nitrogen codoped carbon nanofiber aerogels with optimized electronic structure and enlarged interlayer spacing boost potassium-ion storage, Small 15 (2019) 1900816, https://doi.org/10.1002/smll.201900816.

[46] F. Yuan, Z. Wu, S. Zhang, Z. Li, Q. Wang, H. Sun, D. Zhang, W. Wang, B. Wang, Halide-mediated endogenous ZnO domain-confined etching strategy: realizing superior potassium storage in carbon anode, J. Colloid Interface Sci. 659 (2024) 811–820, https://doi.org/10.1016/j.jcis.2024.01.021.

[47] P. Wang, Z. Gong, K. Ye, Y. Gao, K. Zhu, J. Yan, G. Wang, D. Cao, Sulfur-doped biomass carbon as anode for high temperature potassium ion full cells, Electrochim. Acta 374 (2021) 137920, https://doi.org/10.1016/j.electacta.2021.137920.

[48] R. Saroha, J.S. Cho, J.-H. Ahn, Synergetic effects of cation (K+) and anion (S2−)-doping on the structural integrity of Li/Mn-rich layered cathode material with considerable cyclability and high-rate capability for li-ion batteries, Electrochim. Acta 366 (2021) 137471, https://doi.org/10.1016/j.electacta.2020.137471.

[49] G.D. Park, Y.C. Kang, J.S. Cho, Morphological and electrochemical properties of $ZnMn_2O_4$ nanopowders and their aggregated microspheres prepared by simple spray drying process, Nanomaterials 12 (2022) 680, https://doi.org/10.3390/nano12040680.

[50] S.Y. Jeong, S. Ghosh, J.K. Kim, D.W. Kang, S.M. Jeong, Y.C. Kang, J.S. Cho, Multi-channel-contained few-layered $MoSe_2$ nanosheet/N-doped carbon hybrid nanofibers prepared using diethylenetriamine as anodes for high-performance sodium-ion batteries, J. Ind. Eng. Chem. 75 (2019) 100–107, https://doi.org/10.1016/j.jiec.2019.03.007.

[51] K.C. Nam, Y.H. Seon, P. Bandyopadhyay, J.S. Cho, S.M. Jeong, Porous nanofibers comprising hollow Co3O4/Fe3O4 nanospheres and nitrogen-doped carbon derived by fe@ ZIF-67 as anode materials for lithium-ion batteries, Int. J. Energy Res. 46 (2022) 8934–8948, https://doi.org/10.1002/er.7770.

[52] N. Kitchamsetti, D. Kim, A facile method for synthesizing MOF derived $ZnCo_2O_4$ particles on MXene nanosheets as a novel anode material for high performance hybrid supercapacitors, Electrochim. Acta 441 (2023) 141824, https://doi.org/10.1016/j.electacta.2023.141824.

[53] S.H. Oh, J.S. Cho, Hierarchical (ni, Co)Se2/CNT hybrid microspheres consisting of a porous yolk and embossed hollow thin shell for high-performance anodes in sodium-ion batteries, J. Alloy. Compd. 806 (2019) 1029–1038, https://doi.org/10.1016/j.jallcom.2019.07.351.

[54] X. Liu, R. Wang, S. Liu, J. Pu, H. Xie, M. Wu, D.M. Liu, Y. Li, J.W. Liu, Organic eutectic salts-assisted direct lithium regeneration for extremely low state of health ni-rich cathodes, Adv. Energy Mater. 13 (2023) 2302987, https://doi.org/10.1002/aenm.202302987.

[55] L. Wang, J. Yang, J. Li, T. Chen, S. Chen, Z. Wu, J. Qiu, B. Wang, P. Gao, X. Niu, H. Li, Graphite as a potassium ion battery anode in carbonate-based electrolyte and ether-based electrolyte, J. Power Sources 409 (2019) 24–30, https://doi.org/10.1016/j.jpowsour.2018.10.092.

[56] K. Yang, W. Zhou, Q. Fu, L. Xiao, Y. Mo, J. Ke, W. Shen, Z. Wang, J. Tu, S. Chen, P. Gao, J. Liu, Optimizing kinetics for enhanced potassium-ion storage in carbon-based anodes, Adv. Funct. Mater. 33 (2023) 2306190, https://doi.org/10.1002/adfm.202306190.